VNU Journal of Science: Mathematics - Physics
Journal homepage: https://js.vnu.edu.vn/MaP

Original Article

Structural Properties of $CuFe_2O_4$/ZnO Nanocomposite: Insights from X-ray Diffraction and Extended X-ray Absorption Fine Structure

To Thanh Loan[1,2,*], Tran Thi Viet Nga[1,2], Nguyen Kim Thanh[3]

[1]*International Training Institute for Materials Science (ITIMS), Hanoi University of Science and Technology (HUST), 1 Dai Co Viet, Hanoi, Vietnam*
[2]*School of Materials Science and Engineering, Hanoi University of Science and Technology (HUST), 1 Dai Co Viet, Hanoi, Vietnam*
[3]*Le Quy Don University of Science and Technology, 236 Hoang Quoc Viet 236, Hanoi, Vietnam*

Received 28 July 2024
Revised 28 August 2024; Accepted 10 December 2024

Abstract: This work presents a comprehensive study of the structural properties of a $CuFe_2O_4$/ZnO nanocomposite, with a $CuFe_2O_4$/ZnO ratio of 1:1. $CuFe_2O_4$/ZnO nanocomposite was synthesized using a two-step co-precipitation method. First, $CuFe_2O_4$ nanoparticles were prepared using the spray co-precipitation technique, then the nanoparticles were modified by sodium citrate and coated with ZnO. The structural parameters of both the crystal and local structures of the $CuFe_2O_4$ constituent within the nanocomposite were obtained by using a combination of X-ray diffraction (XRD) and extended X-ray absorption fine structure (EXAFS) analyses. The obtained results indicated that both the crystal and local structures of the $CuFe_2O_4$ constituent in the nanocomposite form are not affected by the ZnO coating. The $CuFe_2O_4$ constituent has a cubic spinel structure with 15% of Cu^{2+} ions distributed in the tetrahedral sites. Interatomic distances have been identified both as averages and specifically around Fe and Cu atoms to determine any sub-lattice distortion and the formation of distinct sub-lattices around Fe and Cu atoms in the cubic structure.

Keywords: Nanocomposite, nanoparticle, crystal structure, local structure, EXAFS.

1. Introduction

Copper ferrite ($CuFe_2O_4$) is one of the most important spinel ferrites, consistently attracting attention from scientists due to its intriguing physical properties and wide applicability across various fields such

* Corresponding author.
E-mail address: loan.tothanh@hust.edu.vn

https//doi.org/10.25073/2588-1124/vnumap.4959

as biomedicine, sensors, and environmental applications [1-4]. Recently, there has been growing interest in nanocomposite systems consisting of $CuFe_2O_4$ and other materials, including ZnO. Lu et al. [5] demonstrated that $CuFe_2O_4$/ZnO acts as a photocatalyst, effectively operating under visible-light irradiation. This efficiency is attributed to the combination of the p-type semiconductor $CuFe_2O_4$ with the n-type semiconductor ZnO to form a p-n heterojunction photocatalyst. Up to now, $CuFe_2O_4$/ZnO nanocomposites have been continuously fabricated using various methods, such as hydrothermal [6], co-precipitation [7, 8], and others [9-11]. These nanocomposites have shown practical applications in many fields, including electromagnetic wave absorption [7], fuel cells [10], and especially photocatalysis under sunlight [6, 9, 11]. Owing to the magnetism of $CuFe_2O_4$, the nanocomposites can be easily recovered after the reaction and reused. The magnetism of $CuFe_2O_4$ is determined by its structural characteristics.

The crystalline structure of copper ferrite is exceptional compared to other spinel ferrites. Specifically, $CuFe_2O_4$ can exist in two symmetrical forms: cubic (c- $CuFe_2O_4$) and tetragonal (t-$CuFe_2O_4$), wherein Fe and Cu ions are distributed across two tetrahedral and octahedral sites. A general formula of copper ferrite can be written as $(Cu_xFe_{1-x})_A[Cu_{1-x}Fe_{1+x}]_BO_4$, where $(Cu_xFe_{1-x})_A$ and $[Cu_{1-x}Fe_{1+x}]_B$ represent, respectively, the tetrahedral (A) and octahedral [B] sites of the spinel-type structure. The fraction of Fe^{3+} cations occupied in the tetrahedral site, (1-*x*), is called the inversion parameter. In its bulk form, $CuFe_2O_4$ is an inverse spinel ferrite with Cu ions completely occupying the octahedral [B] positions. The cubic phase exists at above 700 K, below this temperature, the material transforms to the tetragonal phase [12]. When the particle size decreases to the nanometer scale, Cu ions can occupy more tetrahedral positions, resulting in $CuFe_2O_4$ becoming a mixed spinel. Consequently, the symmetry in their structure changes, favouring the cubic phase to exist at room temperature [13]. These symmetry and cation distribution changes significantly impact the physical properties of $CuFe_2O_4$, such as magnetism and gas sensitivity [14, 15]. By changing the incorporated materials as well as the fabrication methods and conditions, the structural behaviors of copper ferrite nanoparticles can be modified [4, 16, 17]. Therefore, to control the properties of $CuFe_2O_4$-based nanocomposites for specific applications, in-depth studies of the structure are necessary.

There have been several publications on the structure of $CuFe_2O_4$-based nanocomposites, however, the number is very limited [18-20]. Recently, by using a combination of X-ray diffraction (XRD) and absorption techniques, Caddeo et al., discovered the presence of two different sub-lattices within the crystal structure of $CuFe_2O_4$ phase in $CuFe_2O_4/SiO_2$ nanocomposite synthesized by sol-gel method [20]. In particular, the diffraction spectroscopy indicated that the $CuFe_2O_4$ phase in the nanocomposite is complete inverse spinel and has tetragonal symmetry. Extended X-ray absorption fine structure (EXAFS) spectroscopy showed two different sub-lattices presented within the structure, one tetragonal and one cubic, defined by Cu^{2+} and Fe^{3+} ions, respectively. This is evidence that the Jahn-Teller distortion, which occurs on the Cu^{2+} ions located in octahedral sites, does not affect the coordination geometry of the Fe^{3+} ions, regardless of their location in octahedral or tetrahedral sites. This demonstrates the ability to study the Cu and Fe local environments separately. However, up to now, there has been no publication on the local structure of $CuFe_2O_4$-based nanocomposites where $CuFe_2O_4$ has cubic symmetry.

This work presents a detailed study of the structure of $CuFe_2O_4$/ZnO nanocomposites synthesized by a two-step co-precipitation method, firstly $CuFe_2O_4$ nanoparticles were prepared using the spray co-precipitation method. The morphology, crystalline structure, and magnetic properties of the copper ferrite nanoparticles were reported previously [13]. $CuFe_2O_4$ nanoparticles as shown, possess a mixed spinel structure with cubic symmetry. In this work, we focus on applying a combination of XRD and EXAFS analyses to determine both the crystalline and local structures of the $CuFe_2O_4$ in the nanocomposite samples.

2. Experimental

2.1. Sample Preparation

$CuFe_2O_4$/ZnO nanocomposite samples were synthesized using a two-step co-precipitation method. Firstly, the $CuFe_2O_4$ nanoparticles were prepared by spray co-precipitation method at temperature of 900 °C, as described in [13]. Then, these nanoparticles were modified by sodium citrate and coated with ZnO using the co-precipitation method, following the procedure described in [21]. The ion ratio from the initial chemicals was controlled to ensure a weight ratio of ZnO/$CuFe_2O_4$ equal to 1:1.

2.2. Characterization

XRD measurements of the $CuFe_2O_4$/ZnO nanocomposites were performed on the SmartLab Rigaku X-ray diffractometer with Cu K_α radiation. The XRD data were sequentially analyzed using SmartLab Studio II and FullProf software. Initially, SmartLab Studio II was employed for phase identification, followed by applying FullProf software to refine the crystal structure using the Rietveld method. The diffraction peaks were modeled using the pseudo-Voigt function [22]. The quality of refinement fitting was assessed based on the goodness of fit (χ^2), which ideally approaches one, and the weighted profile *R*-factor (*R*wp), which should be less than 10% [23].

X-ray absorption spectroscopy (XAS) measurements were performed at Beamline 8 of Synchrotron Light Research Institute (Thailand) [24]. The X-ray beam from the synchrotron source has an initial intensity I_0 and an energy varying around the core electron excitation energy of the absorbing atom, passing through a sample of thickness *t*, as depicted in Fig. 1. The X-ray absorption process follows the Beer-Lambert law:

$$I_1 = I_0 e^{-\mu t} \quad (1)$$

where I_1 is the X-ray intensity transmitted through the sample, and μ is the X-ray absorption coefficient.

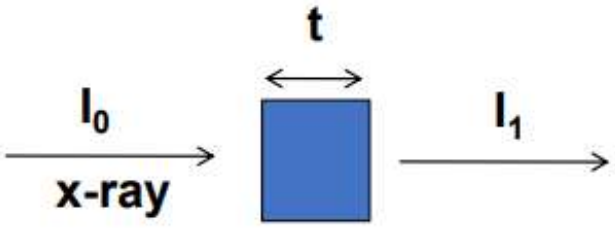

Figure 1. X-ray absorption experiment.

The EXAFS spectra of the $CuFe_2O_4$ nanoparticles and $CuFe_2O_4$/ZnO nanocomposite were collected at the Fe*K*-edge and Cu*K*-edge in transmission mode at room temperature using a Ge (220) double-crystal monochromator. Fe and Cu foil standards were used for photon energy calibration. The EXAFS spectra were collected up to 14.8 $Å^{-1}$ in the wave vector *k* range. The EXAFS data were analyzed using the Athena and Artemis programs [25]. Initially, the Athena program was used to sum the data, identify the absorption edge energy, subtract the background, and obtain the normalized spectra, $\chi(E)$. The normalized EXAFS spectra were then transformed to *k*-space and multiplied by k^3. Subsequently, the k^3-weighted $\chi(k)$ spectra were Fourier transformed to *R*-space. The local structure analysis was performed in the *R*-space fitting mode using the Artemis program by fitting the experimental data with the theoretical model generated by the FEFF code, based on the crystal structure information obtained from XRD analyses. The quality of the EXAFS fit was evaluated by the *R*-factor.

3. Results and Discussion

3.1. Crystalline Structure

XRD patterns of the $CuFe_2O_4$/ZnO nanocomposite and their Rietveld refinement are shown in Fig. 2. The Rietveld refinement result indicated that the nanocomposite contains only $CuFe_2O_4$ phase, with a weight content of 46.7 %, and tZnO phase, with a weight content of 53.3 %. The calculated phase content ZnO/$CuFe_2O_4$ ratio is of approximately 1:1, aligning well with the input initial chemicals. In the nanocomposite, the ZnO phase crystallizes in a hexagonal structure (space group $P6_3mc$) with zinc ions in position (1/3, 2/3, 0) and oxygen in (1/3, 2/3, 0.3850). The lattice parameters of the ZnO phase were determined to be a = 3.2509 ± 0.0007 Å and c = 5.2090 ± 0.0006 Å. The obtained result is in good agreement with the crystalline structure of ZnO reported in [21]. Meanwhile, the $CuFe_2O_4$ phase crystallizes in a spinel structure with cubic symmetry (space group $Fd3m$), in which Cu and Fe ions distribute between (A)-site 8a (1/8, 1/8, 1/8) and [B]-site 16d (1/2, 1/2, 1/2), with the cation distribution of $(Cu_{0.15}Fe_{0.85})_A[Fe_{1.15}Cu_{0.85}]_B$. In this spinel structure, oxygen ions occupy 32e (x, x, x), x = 0.251 ± 0.002. The lattice parameter of $CuFe_2O_4$ phase was found to be a = 8.3765 ± 0.0006 Å. The crystalline structure of the $CuFe_2O_4$ phase is similar to that of the copper ferrite nanoparticles reported previously [13]. Interatomic distances within the first nearest-neighbor coordination sphere were calculated based on the refined structural parameters, as listed in Table 1.

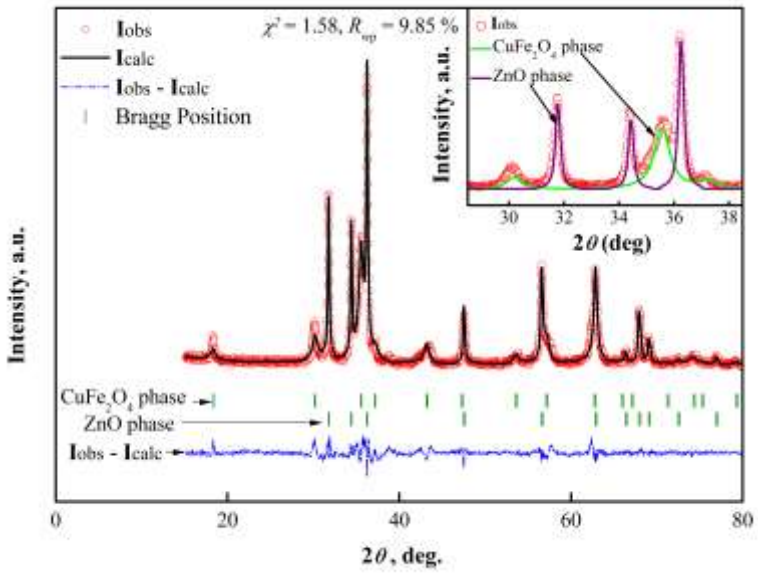

Figure 2. XRD pattern of the $CuFe_2O_4$/ZnO nanocomposite and processed by the Rietveld method. The experimental points as well as calculated and difference functions are indicated. The inset illustrates the contributions to the intensity from $CuFe_2O_4$ and ZnO phases in the 2θ range from 28.5° to 38.5°.

Table 1. Interatomic distances in Å between oxygen ions and cations in A-site and B-site calculated from XRD analyses. Statistical errors are indicated in the last significant digit

$d_{A–O}$	$d_{B–O}$	$d_{B–B}$	$d_{A–A}$	$d_{A–B}$
1.8281(1)	2.0858(1)	2.96154	3.62713(1)	3.47271

3.2. Local Structure

The normalized EXAFS spectra, χ(E), of the $CuFe_2O_4$ nanoparticles and $CuFe_2O_4$/ZnO nanocomposite, measured at the Fe *K*-edge and Cu *K*-edge, are presented in Fig. 3. The spectra for both samples at each absorption edge exhibit similar features. Due to the rapid decay of $\chi(k)$ along the wave vector *k*, the oscillations are amplified by multiplying by k^3. The $k^3\chi(k)$ spectra at the Fe *K*-edge and Cu *K*-edge of the investigated samples, shown in Figure 4, illustrate the fluctuations of the EXAFS signals as functions of the wave vector. At both measured edges, the spectra of the samples overlap, implying a similarity in their local structures around the iron and copper atoms.

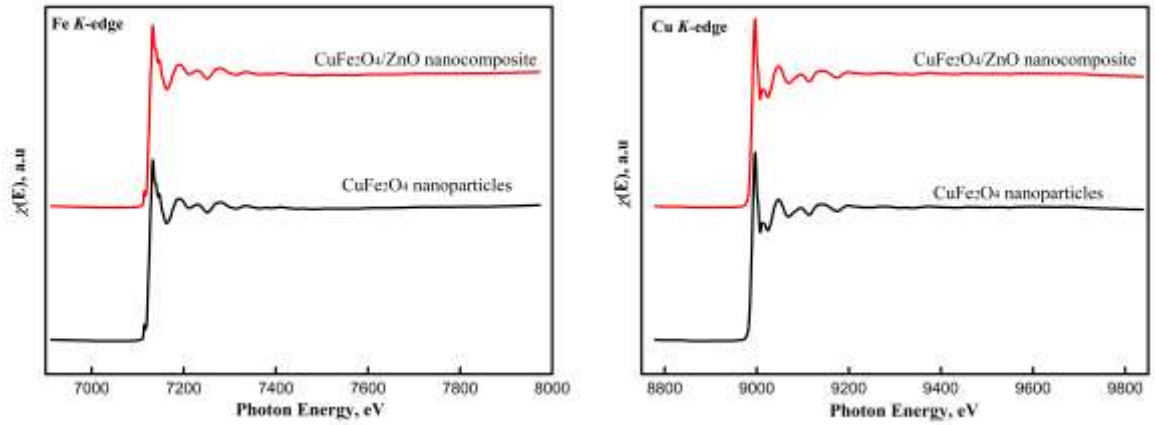

Figure 3. Normalized Fe and Cu *K*-edges EXAFS spectra of the $CuFe_2O_4$ nanoparticles and $CuFe_2O_4$/ZnO nanocomposite.

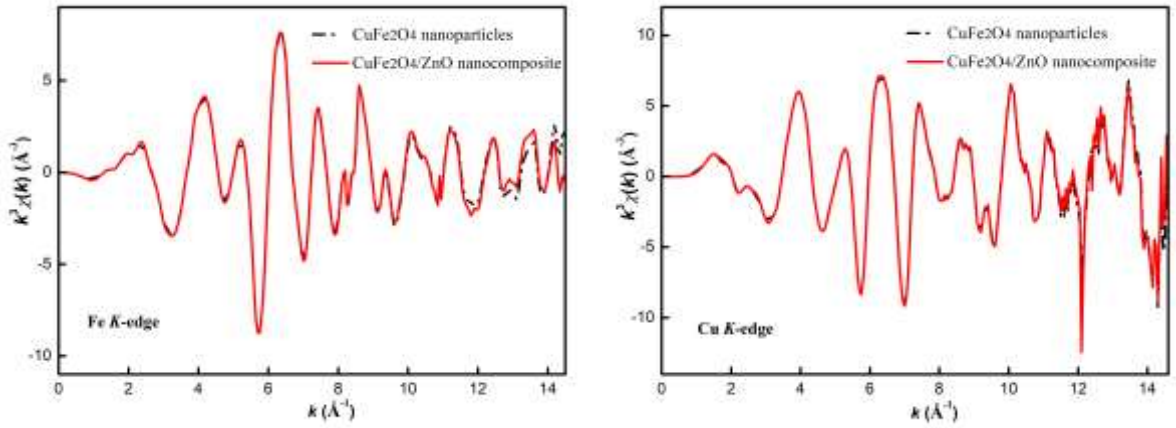

Figure 4. The $k^3\chi(k)$ EXAFS spectra at the Fe and Cu *K*-edges of the $CuFe_2O_4$ nanoparticles and $CuFe_2O_4$/ZnO nanocomposite.

Radial structure functions (RSF) illustrated in Fig. 5 were obtained by Fourier transforming (FT) the k^3-weighted EXAFS spectra from *k*-space to R-space within the *k* range of 3 – 12 $Å^{-1}$. The RSF represents the signal intensity as a function of the distance from the absorbing atom to neighboring atoms. In the RSF profiles, the peaks correspond to the most probable distances from the absorbing atom

(Fe/Cu) to the surrounding neighboring atoms. The RSF profiles at both the Fe *K*-edge and Cu *K*-edge show four main peaks below 4 Å. At the Fe *K*-edge, the first peak at approximately 1 Å corresponds to iron coordinated to oxygen in the tetrahedral site, the second peak at approximately 1.6 Å corresponds to iron coordinated to oxygen in the octahedral site, the third peak at approximately 2.7 Å corresponds to the iron-metal distance (Fe-M) between neighboring octahedral sites, and the fourth peak at approximately 3.1 Å corresponds to the iron-metal distance between neighboring octahedral and tetrahedral sites [26]. Similarly, at the Cu *K*-edge, four peaks below 4 Å correspond to the bonds between Cu atoms and their neighboring atoms. The peak at approximately 1 Å observed in all the RSF profiles is evidence that both Fe and Cu ions are distributed in tetrahedral positions.

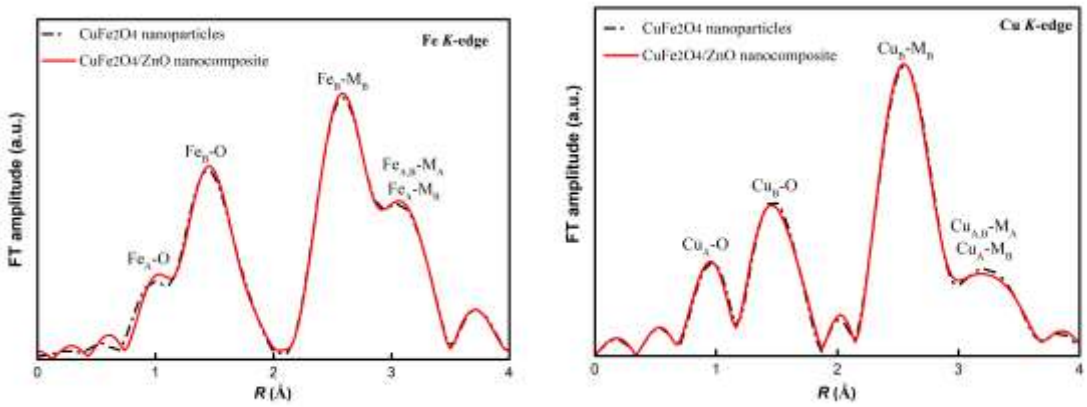

Figure 5. Fourier transforms of the Fe and Cu *K*-edges EXAFS spectra of the $CuFe_2O_4$ nanoparticles and $CuFe_2O_4$/ZnO nanocomposite.

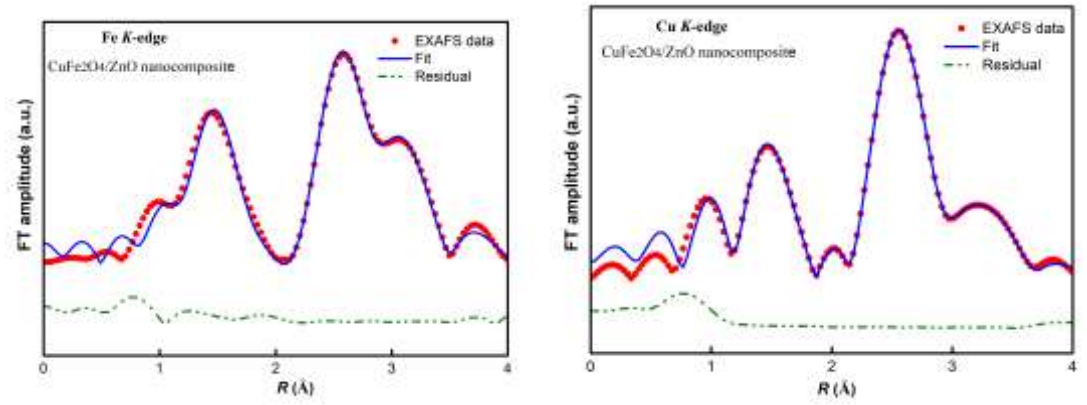

Figure 6. Fourier transforms of Fe and Cu *K*-edge EXAFS spectra compared to their best-fit for the $CuFe_2O_4$/ZnO nanocomposite. The residuals between the data and fitting are shown.

The EXAFS data were fitted using a theoretical model based on the structural parameters obtained from the Rietveld refinement to identify the local environment around the absorbing atoms (iron and copper) in the structure. The model includes single scattering paths from the two sites within 4 Å of the central absorbing atom sites, i.e., the first Fe–O/Cu–O and the second Fe–M/Cu–M coordination shells. The experimental Fourier transform and its best fit are presented in Fig. 6 for the $CuFe_2O_4$/ZnO nanocomposite at the Fe and Cu *K*-edge.

Table 2. Parameters of the local structure of the $CuFe_2O_4$ nanoparticles and $CuFe_2O_4$/ZnO nanocomposite samples at the Fe *K*-edge. *N* is the coordination number; *R* is interatomic distances and σ^2 is the Debye-Waller factor. Statistical errors are indicated in the last significant digit

Sample		$CuFe_2O_4$ nanoparticles		$CuFe_2O_4$/ZnO nanocomposite	
	N	*R*, Å	σ^2, Å^2	*R*, Å	σ^2, Å^2
Fe–O	4	1.8984(6)	0.0013(4)	1.8975(8)	0.0016(5)
Fe–O	6	2.0199(6)	0.0044(4)	2.0129(5)	0.0045(3)
Fe–Fe	6	2.9508(1)	0.0006(4)	2.9518(6)	0.0006(7)
Fe–Fe	4	3.3696(2)	0.0164(5)	3.3705(5)	0.0161(1)
Fe–Cu	6	3.5183(8)	0.0138(6)	3.5176(7)	0.0144(6)
Fitting quality		*R*-factor = 0.58 %		*R*-factor = 0.68 %	

Table 3. Parameters of the local structure of the $CuFe_2O_4$ nanoparticles and $CuFe_2O_4$/ZnO nanocomposite samples at the Cu *K*-edge. *N* is the coordination number; *R* is interatomic distances and σ^2 is the Debye-Waller factor. Statistical errors are indicated in the last significant digit

Sample		$CuFe_2O_4$ nanoparticles		$CuFe_2O_4$/ZnO nanocomposite	
	N	*R*, Å	σ^2, Å^2	*R*, Å	σ^2, Å^2
Cu–O	4	1.9739(9)	0.0082(1)	1.9744(7)	0.0081(1)
Cu–O	6	2.1934(8)	0.0025(1)	2.1942(9)	0.0032(1)
Cu–Cu	6	2.9523(6)	0.0039(1)	2.9513(8)	0.0041(1)
Cu–Cu	4	3.9628(6)	0.0035(3)	3.9637(5)	0.0036(3)
Cu–Fe	6	3.4352(9)	0.0138(7)	3.4346(8)	0.0132(7)
Fitting quality		*R*-factor = 0.42 %		*R*-factor = 0.59 %	

The fitting results at both Fe and Cu *K*-edges of the $CuFe_2O_4$ nanoparticles and $CuFe_2O_4$/ZnO nanocomposite confirmed the cation distribution of $(Cu_{0.15}Fe_{0.85})_A[Fe_{1.15}Cu_{0.85}]_B$ as determined from Rietveld analysis. Two distributions for the first oxygen coordination shell (Fe–O/Cu–O) and three distributions for the second coordination shell (Fe–M/Cu–M) were identified and are given in Table 2 and Table 3 for Fe and Cu *K*-edges, respectively. The interatomic distances between the absorbing atom (Fe/Cu) and their surrounding atoms in the $CuFe_2O_4$ nanoparticles are similar to those of the $CuFe_2O_4$/ZnO nanocomposite within the corresponding statistical errors, indicating that the local structure of the $CuFe_2O_4$ phase remains unchanged during the ZnO coating process. Although the interatomic distances presented in Table 2 and Table 3 follow the same trend as the average distances calculated from XRD analyses (presented in Table 1), the local structures around Fe and Cu atoms differ. Specifically, the distances from Fe atoms to their nearest neighbors are generally shorter than the corresponding distances from Cu atoms to their nearest neighbors. For example, the Fe–O distance is 1.898 Å at the tetrahedral site, whereas the Cu–O distance is 1.974 Å. This difference can be attributed to the valence states of the copper and iron ions. As indicated in our previous publication [15], the Cu ions in the $CuFe_2O_4$ nanoparticles have a valence state of +2. Additionally, the nanoparticles contain a small amount of Fe^{2+} ions, approximately 6.4%. The Fe^{3+} ions, which have a smaller ionic radius than Cu^{2+} ions, result in shorter interatomic distances from iron ions to their neighbors. However, the small amount of Fe^{2+} ions, which have a larger ionic radius than Cu^{2+} ions and are only distributed in the octahedral sites, leads to a larger Fe–Cu distance compared to the Cu–Fe distance in six-coordination environments. Contrary to the findings of Caddeo et al. on t-$CuFe_2O_4$ [20], no sub-lattice distortion or formation of distinct sub-lattice types around Fe and Cu atoms was observed in the structure of our

investigated samples. This can be explained by the fact that the cubic structure does not exhibit Jahn-Teller distortion, resulting in no distortion within the sub-lattices. Additionally, the sub-lattices have the same symmetry, allowing Cu ions to be distributed in both tetrahedral and octahedral positions.

4. Conclusion

$CuFe_2O_4$/ZnO nanocompositeswere successfully synthesized by a two-step co-precipitation method, where $CuFe_2O_4$ nanoparticle constituent was prepared by the spray co-precipitation method. Comprehensive structural analyses combining XRD and EXAFS confirmed their cubic structure with an inversion degree of 0.85 for $CuFe_2O_4$ in both the nanoparticle and the nanocomposite. ZnO coating process does not affect to both the crystalline structure and local structure of the c-$CuFe_2O_4$. Although the obtained interatomic distances follow the same trend, the local structures around the iron and copper atoms in the c- $CuFe_2O_4$ exhibit differing. Specifically, the distances from Fe atoms to their neighboring atoms are generally shorter than those from Cu atoms to their neighboring atoms. No distinct sub-lattices are formed around Fe and Cu atoms in this cubic spinel structure. These obtained results are significant for studying and evaluating the properties of the nanocomposites based on c-$CuFe_2O_4$.

Acknowledgments

This research is funded by Hanoi University of Science and Technology (HUST) under project number T2022-PC-091.

References

[1] Z. Sun, L. Liu, D. Z. Jia, W. Pan, Simple Synthesis of $CuFe_2O_4$ Nanoparticles as Gas-sensing Materials, Sensors and Actuators B: Chemical, Vol. 125, 2007, pp. 144-148, https://doi.org/10.1016/j.snb.2007.01.050.

[2] S. Park, J. H. Baek, L. Zhang, J. M. Lee, K. H. Stone, I. S. Cho, J. Guo, H. S. Jung, X. Zheng, Rapid Flame-Annealed $CuFe_2O_4$ as Efficient Photocathode for Photoelectrochemical Hydrogen Production, ACS Sustainable Chemistry & Engineering, Vol. 7, 2019, pp. 5867-5874, https://doi.org/10.1021/acssuschemeng.8b05824.

[3] J. Feng, L. Su, Y. Ma, C. Ren, Q. Guo, X. Chen, $CuFe_2O_4$ Magnetic Nanoparticles: A Simple and Efficient Catalyst for the Reduction of Nitrophenol, Chemical Engineering Journal, Vol. 221, 2013, pp. 16-24, https://doi.org/10.1016/j.cej.2013.02.009.

[4] S. M. Fotukian, A. Barati, M. Soleymani, A. M. Alizadeh, Solvothermal Synthesis of $CuFe_2O_4$ and Fe_3O_4 Nanoparticles with High Heating Efficiency for Magnetic Hyperthermia Application, Journal of Alloys and Compounds, Vol. 816, 2020, pp. 152548, https://doi.org/10.1016/j.jallcom.2019.152548.

[5] C. Lu, Z. Bao, C. Qin, L. Dai, A. Zhu, Facile Fabrication of Heterostructured Cubic-$CuFe_2O_4$/ZnO Nanofibers (c-CFZs) with Enhanced Visible-light Photocatalytic Activity and Magnetic Separation, RSC Advances, Vol. 6, 2016, pp. 110155-110163, https://doi.org/10.1039/c6ra23970f.

[6] C. Karunakaran, P. Vinayagamoorthy, J. Jayabharathi, $CuFe_2O_4$-Encapsulated ZnO Nanoplates: Magnetically Retrievable Biocidal Photocatalyst, Journal of Nanoscience and Nanotechnology, Vol. 17, No. 7, 2017, pp. 4489-4497, https://doi.org/10.1166/jnn.2017.14190.

[7] K. Ali, J. Iqbal, T. Jan, I. Ahmad, D. Wan, A. Bahadur, S. Iqbal, Synthesis of $CuFe_2O_4$-ZnO Nanocomposites with Enhanced Electromagnetic Wave Absorption Properties, Journal of Alloys and Compounds, Vol. 705, 2017, pp. 559-565, https://doi.org/10.1016/j.jallcom.2017.01.264.

[8] J. J. Rushmittha, S. Radhika, G. Maheshwaran, C. M. Padma, Tuning the Electrochemical Performance of Binary $CuFe_2O_4$ Incorporated by ZnO Nanoparticles for High Performance Hybrid Supercapacitors, Inorganic Chemistry Communications, Vol. 159, 2024, pp. 111728, https://doi.org/10.1016/j.inoche.2023.111728.

[9] A. S. Arreola, A. M. H. Flores, J. M. M. Hernández, L. M. T. Martínez, Improved Photocatalytic Activity for Water Splitting over MFe_2O_4–ZnO (M = Cu and Ni) Type-ll Heterostructures, Journal of Photochemistry and Photobiology A: Chemistry, Vol. 364, 2018, pp. 433-442, https://doi.org/10.1016/j.jphotochem.2018.06.033.
[10] S. Paydar, N. Akbar, Q. Shi, Y. Wu, Developing Cuprospinel $CuFe_2O_4$–ZnO Semiconductor Heterostructure as a Proton Conducting Electrolyte for Advanced Fuel Cells, International Journal of Hydrogen Energy, Vol. 46, Iss. 15, 2021, pp. 9927-9937, https://doi.org/10.1016/j.ijhydene.2020.04.198.
[11] M. Fedailaine, M. Trari, Photoreduction of Ni^{2+} under Solar and Artificial Reactors on The Hetero-junction ($CuFe_2O_4$/ZnO): Comparison between Experimental and Theoretical Results, Materials Today Communications, Vol. 31, 2022, pp. 103665, https://doi.org/10.1016/j.mtcomm.2022.103665.
[12] A. M. Balagurov, I. A. Bobrikov, M. S. Maschenko, D. Sangaa, V. G. Simkin, Structural Phase Transition in $CuFe_2O_4$ Spinel, Crystallography Reports, Vol. 58, 2013, pp. 710-717, https://doi.org/10.1134/S1063774513040044.
[13] N. K. Thanh, N. P. Duong, D. Q. Hung, T. T. Loan, T. D. Hien, Structural and Magnetic Characterization of Copper Ferrites Prepared by Using Spray Co-Precipitation Method, Journal of Nanoscience and Nanotechnology, Vol. 16, No. 8, 2016, pp. 7949-7954, https://doi.org/10.1166/jnn.2016.12750.
[14] L. N. Anh, T. T. Loan, N. K. Thanh, N. P. Duong, D. T. T. Nguyet, N. M. Hong, Structural and H_2S Sensing Properties of Copper Ferrite Nanoparticles Prepared Through Hydrothermal Method, Journal of Nanoscience and Nanotechnology, Vol. 21, No. 4, 2021, pp. 2641-2646, https://doi.org/10.1166/jnn.2021.19095.
[15] N. K. Thanh, T. T. Loan, L. N. Anh, N. P. Duong, S. Soontaranon, N. Thammajak, T. D. Hien, Cation Distribution in $CuFe_2O_4$ Nanoparticles: Effects of Ni Doping on Magnetic Properties, Journal of Applied Physics, Vol. 120, 2016, pp. 142115, https://doi.org/10.1063/1.4961722.
[16] R. Khunphonoi, P. Khemthong, C. Luadthong, S. Kuboon, C. Kongmark, N. V. Empikul, P. Kidkhunthod, S. Pinitsoontorn, K. Faungnawakij, Correlating The Effect of Preparation Methods on The Structural and Magnetic Properties, and Reducibility of $CuFe_2O_4$ Catalysts, RSC Advances, Vol. 12, 2022, pp. 15526-15533, https://doi.org/10.1039/d2ra01708c.
[17] T. F. Marinca, I. Chicinaş, O. Isnard, Synthesis, Structural and Magnetic Characterization of Nanocrystalline $CuFe_2O_4$ as Obtained by a Combined Method Reactive Milling, Heat Treatment and Ball Milling, Ceramics International, Vol. 38, Iss. 3, 2012, pp. 1951-1957, https://doi.org/10.1016/j.ceramint.2011.10.026.
[18] V. Krishnan, R. K. Selvan, C. O. Augustin, EXAFS and XANES Investigations of $CuFe_2O_4$ Nanoparticles and $CuFe_2O_4$ - MO_2 (M = Sn, Ce) Nanocomposites, The Journal of Physical Chemistry C, Vol. 111, Iss. 45, 2007, pp. 16724-16733, https://doi.org/10.1021/jp073746t.
[19] R. K. Selvan, V. Krishnan, C. O. Augustin, H. Bertagnolli, C .S. Kim, A. Gedanken, Investigations on the Structural, Morphological, Electrical, and Magnetic Properties of $CuFe_2O_4$-NiO Nanocomposites, Chemistry of Materials, Vol. 20, Iss. 2, 2008, pp. 429-439, https://doi.org/10.1021/cm701937q.
[20] F. Caddeo, D. Loche, M. F. Casula, A. Corrias, Evidence of A Cubic Iron Sub-lattice in t-$CuFe_2O_4$ Demonstrated by X-ray Absorption Fine Structure, Scientific Reports, Vol. 8, No. 797, 2018, https://doi.org/10.1038/s41598-017-19045-8.
[21] T. T. Loan, D. K. Huy, H. M. Chung, N. K. Thanh, T. D. Hoan, N. P. Duong, S. Soontaranon, W. Klysubun, Structure and Magnetic Properties of Magnetic Iron Oxide/Zinc Oxide Core/shell Nanocomposites: Effect of ZnO Coating, Materials Today Communications, Vol. 26, 2021, pp. 101733, https://doi.org/10.1016/j.mtcomm.2020.101733.
[22] D. Balzar, Voigt-Function Model in Diffraction Line-Broadening Analysis, Defects and Microstructure Analysis by Diffraction, International Union of Crystallography, Monograph on Crystallography, Oxford University Press, Oxford, UK, 1999, pp. 94-126.
[23] L. B. McCusker, R. B. V. Dreele, D. E. Cox, D. Louër, P. Scardi, Rietveld Refinement Guidelines, Journal of Applied Crystallography, Vol. 32, 1999, pp. 36-50, https://doi.org/10.1107/S0021889898009856.
[24] W. Klysubun, P. Sombunchoo, W. Deenan, C. Kongmark, Performance and Status of Beamline BL8 at SLRI for X-ray Absorption Spectroscopy, Journal of Synchrotron Radiation, Vol. 19, 2012, pp. 930-936, https://doi.org/10.1107/S0909049512040381.
[25] B. Ravel, M. Newville, Athena, Artemis, Hephaestus: Data Analysis for X-ray Absorption Spectroscopy using IFEFFIT, Journal of Synchrotron Radiation, Vol. 12, 2005, pp. 537-541, https://doi.org/10.1107/S0909049505012719.
[26] C. M. B. Henderson, J. M. Charnock, D. A. Plant, Cation Occupancies in Mg, Co, Ni, Zn, Al Ferrite Spinels: A Multi-element EXAFS Study, Journal of Physics: Condensed Matter, Vol. 19, 2007, pp. 076214, https://doi.org/10.1088/0953-8984/19/7/076214.